ELSEVIER

Journal of Fluids and Structures 19 (2004) 863–879

JOURNAL OF FLUIDS AND STRUCTURES

www.elsevier.nl/locate/jnlabr/yjfls

A study of double flutter

P.A. Chamara[a], B.D. Coller[b,*]

[a] *Department of Mechanical Engineering, University of Illinois at Chicago, Chicago, IL 60607-7022, USA*
[b] *Department of Mechanical Engineering, Northern Illinois University, DeKalb, IL 60115, USA*

Received 22 November 2001; accepted 12 May 2004

Available online 06 August 2004

Abstract

We study nonlinear flutter phenomena in a system of two airfoils in close proximity in an ideal fluid. In particular, we are interested in cases for which two aeroelastic instabilities are nearly critical simultaneously. Such Hopf–Hopf interactions, in general, are capable of generating a rich variety of dynamic phenomena, behaviors that possibly can be exploited to develop flow actuators. Our first task is to investigate the degree to which the double Hopf interactions are prevalent in the physical system. Secondly, using tools of center manifolds and normal forms, we investigate the richness of the dynamics in the two airfoil system. Analysis is facilitated by an effective reduced-order modeling effort.
© 2004 Published by Elsevier Ltd.

1. Introduction

Mathematically speaking, a traditional oscillatory flutter instability corresponds to a single complex conjugate pair of eigenvalues of the linearized system crossing the imaginary axis transversely as a parameter (e.g., flow speed) varies. In the terminology of nonlinear dynamical systems, this is a Hopf bifurcation. The term "double flutter" in the paper's title refers to aeroelastic instabilities for which two complex conjugate pairs of eigenvalues cross the imaginary axis (nearly) simultaneously: Hopf–Hopf bifurcations. Chamara and Coller (2000) demonstrated that such coincident instabilities exist in systems with two airfoils in close proximity. The configuration, depicted in Fig. 1, is the problem we continue to pursue here. Double flutter is not limited to the two airfoil problem. Other instances include a single airfoil with elastic control surface (Tang et al., 1998), and panel flutter (Dowell, 1975).

Double flutter interests us on several levels. The first is an intrinsic curiosity in nonlinear aeroelastic phenomena. Hopf–Hopf interactions in general tend to yield rich dynamics: 132 distinct behaviors are entangled in the generic cubic order normal form. Some subsets of these are likely to play important roles in the nonlinear interactions of the two airfoils.

From a practical perspective, we are interested in the double flutter problem because the rich nonlinear dynamics might provide a means for creating a new generation of passive or semi-active flow control actuators. The Kelvin–Helmholtz instability and subsequent roll-up dynamics of the shear layer in the wake can provide an effective means of mixing passive scalars and momentum. The airfoils and their wakes may also be used to interact with separating shear layers. Whereas small, sinusoidally actuated, flaps have been used in the past to dramatically improve pressure recovery in diffusers (McKinzie, 1991,1996), the natural limit cycle dynamics associated with aeroelastic instability may provide a similar effect. However, instead of supplying energy to the controller, fluttering airfoil actuators would extract their energy from the flow. In fact, the rich dynamics might provide a range of multi-frequency

*Corresponding author.
E-mail address: coller@ceet.niu.edu (B.D. Coller).

0889-9746/$ - see front matter © 2004 Published by Elsevier Ltd.
doi:10.1016/j.jfluidstructs.2004.05.002

Nomenclature

Subscripts j denote quantities associated with the jth blade

Physical parameters

h_j	vertical displacement of elastic axis (positve upward)
α_j	airfoil pitch (positive nose up)
t	time
b_j	half the airfoil chord
d	blade spacing
ρ	fluid density per unit depth
m_j	mass of airfoil
I_{ea_j}	moment of inertia about elastic axis
	$-[k_{h_j1}h + k_{h_j2}h^2 + k_{h_j3}h^3]$ restoring force of plunge spring
	$-[k_{\alpha_j1}\alpha + k_{\alpha_j2}\alpha^2 + k_{\alpha_j3}\alpha^3]$ restoring force of pitch spring
ω_{h_j}	uncoupled natural plunge frequency $(= \sqrt{k_{h_j1}/m})$
ω_{α_j}	uncoupled natural pitch frequency $(= \sqrt{k_{\alpha_j1}/I_{ea_j}})$
V_j	potential function for restoring forces
L_j	aerodynamic lift
M_{ea_j}	aerodynamic moment about elastic axis

Dimensionless parameters

β_j	chord ratio $(= b_j/b_1)$
$\tilde{d}$	dimensionless blade spacing $(= d/b_1)$
$\tilde{h_j}$	normalized displacement airfoil displacement $(= h_j/b_j)$
$\chi_j b_j$	location of center of mass of airfoil aft of the elastic axis
$\xi_{ea_j} b_{j1}$	location of the elastic axis aft of the leading edge
τ	dimensionless time $(= \omega_{\alpha 1} t)$
δ_{h_j2}	quadratic plunge spring coefficient $(= bk_{h_j2}/k_{h_j1})$
δ_{h_j3}	cubic plunge spring coefficient $(= b^2 k_{h_j3}/k_{h_j1})$
δ_{α_j2}	quadratic pitch spring coefficient $(= k_{\alpha_j2}/k_{\alpha j}1)$
δ_{α_j3}	cubic pitch spring coefficient $(= k_{\alpha_j3}/k_{\alpha j}1)$
X_j	ratio of uncoupled natural frequency $(= \omega_{h_j}/\omega_{\alpha_j})$
Y_j	interblade frequency ratio $(= \omega_{\alpha_j}/\omega_{\alpha_1})$
μ_j	mass ratio $(= m_j/\pi\rho b_j^2)$
r_{α_j}	dimensionless radius of gyration $(= I_{ea_j}/m_j b_j^2)$
$\tilde{V_j}$	dimensionless potential $(= V_j/k_{\alpha_j1})$
$\tilde{U}$	dimensionless flow speed $(= U/b_{1\omega_{\alpha_1}})$
$\tilde{L_j}$	dimensionless lift $(= L_j/\pi\rho b_j U^2)$
$\tilde{M}_{ea_j}$	dimensionless moment about elastic axis $(= M_{ea_j}/\pi\rho U^2)$

and pulse-like behaviors that have been demonstrated to be particularly effective in flow control problems (Parekh and Glezer, 2000; Glezer 2000).

Hopf–Hopf bifurcations also occur in surge and rotating stall interactions in axial compressors (Coller, 2004), roll-coupling instabilities of high angle of attack aircraft dynamics (Jahnke and Culick 1994), coupled chemical oscillators (Wang and Nicolis, 1987), rotating shafts (Shaw and Shaw, 1989), and combustion instabilities due to coupling of acoustic modes to heat release (Murray et al., 1997) to name just a few. Double flutter might provide a more practical test-bed for developing generally applicable Hopf–Hopf case-seeking and identification techniques.

In this study, we shall seek answers to two general questions regarding double flutter in the two airfoil system. First, we shall perform linear analyses to gain a feel for the prevalence or scarcity of double Hopf bifurcations. In the second part, we investigate nonlinear phenomena that occur in the vicinity of the aeroelastic Hopf–Hopf bifurcations, ascertaining which of the possible 132 behaviors actually occur in models of the physical system. Qualitative predictions based on a reduced-order model are verified with high fidelity simulations.

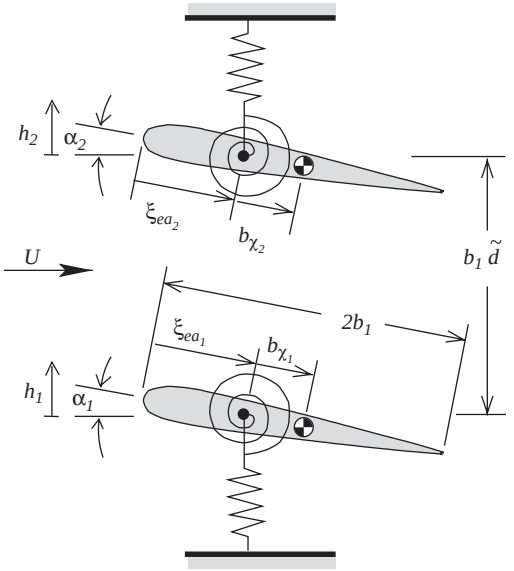

Fig. 1. The system of two airfoils.

2. Modeling

In our study of double flutter, we shall consider a system of two airfoils elastically suspended in a two-dimensional, nominally uniform flow of an inviscid and incompressible fluid. Each has two degrees of freedom: pitch and plunge. They are coupled only through the fluid. An illustration is provided and several physical parameters are labeled in Fig. 1. While, in general, there may be stagger and the blades may be of different sizes, we shall only consider size ratio $\beta_2 := b_2/b_1 \equiv 1$, and zero stagger angle in this paper.

One may trivially create a Hopf–Hopf bifurcation by choosing identical airfoils with spacing, $\tilde{d}$, sufficiently large that the blades are effectively uncoupled. However, since it is the dynamic interactions of the two oscillatory instabilities that interest us, we choose the spacing relatively small so that there is strong aerodynamic coupling between the blades.

As in our previous nonlinear analysis of single blade flutter (Coller and Chamara, 2004), the tools of center manifolds and normal forms we shall employ require that we represent the dynamics of the system as a relatively low-order system of ordinary differential equations in the time domain. After scaling, we express the equations of motion as

$$\begin{aligned} &\tilde{h}_j'' - \chi_j \cos(\alpha_j)\alpha_j'' + \chi_j \sin(\alpha_j)\alpha_j' 2 + r_{\alpha_j}^2 Y_j^2 \frac{\partial \tilde{V}_j}{\partial \tilde{h}_j} = \frac{\tilde{U}^2}{\mu_j \beta_j^2} \tilde{L}_j, \\ &-\chi_j \cos(\alpha_j)\tilde{h}_j'' + r_{\alpha_j}^2 \alpha_j'' + r_{\alpha_j}^2 Y_j^2 \frac{\partial \tilde{V}_j}{\partial \alpha_j} = \frac{\tilde{U}^2}{\mu_j \beta_j^2} \tilde{M}_{ea_j}, \end{aligned} \tag{1}$$

where the index j refers to the jth blade. Prime denotes differentiation with respect to dimensionless time, $\tau = \omega_{\alpha_1} t$. Other nondimensionalizations are listed in the nomenclature and depicted in Fig. 1.

As in Coller and Chamara (2004), we shall consider relatively small airfoil motions so that the aerodynamic lifts $\tilde{L}_j$ and moments about the elastic axis $\tilde{M}_{ea_j}$ respond linearly to blade motions and their history. Consequently, the inertial nonlinearities in Eq. (1) vanish: $\cos(\alpha) \approx 1$, $\sin(\alpha)\alpha'^2 \approx 0$. This leaves the only nonlinearity in the elastic restoring forces whose potential is given by

$$\tilde{V}_j = \frac{X_j^2}{r_{\alpha_j}^2}\left[\frac{1}{2}\tilde{h}_j^2 + \frac{1}{3}\delta_{h2}\tilde{h}_j^3 + \frac{1}{4}\delta_{h3}\tilde{h}_j^4\right] + \frac{1}{2}\alpha_j^2 + \frac{1}{3}\delta_{\alpha 2}\alpha_j^3 + \frac{1}{4}\delta_{\alpha 3}\alpha_j^4. \tag{2}$$

The aerodynamic lifts and moments are the result of infinite-dimensional processes. Nonetheless, it is well known that the forces may be well modelled with relatively low-order systems. As we describe below, we use rather simple lag models to fit the step response and frequency response data from a high fidelity vortex lattice simulation.

We express aerodynamic forces such as lift as a sum of two different types of terms: $\tilde{L}_j = \tilde{L}_j^{(M)} + \tilde{L}_j^{(C)}$. The superscript (M) denotes a set of "memoryless" terms, mostly of apparent mass origin, which are linear functions of accelerations. The (C) superscript refers to terms that tend to be of circulatory type. For a single airfoil, Fung (1993) writes this circulatory part as a Duhamel integral which convolves Wagner's function, Φ, with $\tilde{W}'^{(m)}_{3/4}$, the time derivative of a component of upwash at the $\frac{3}{4}$ -chord location due to blade motion. The superscript (m) denotes that component of upwash due to blade motion in a uniform free-stream.

In the two airfoil problem, we mold the aerodynamic response into a similar formulation. One major difference, however, is that, for the two airfoil problem, we know of no privileged location such as the $\frac{3}{4}$ -chord point which conveys all the necessary information. Therefore, we must consider the distribution of upwash over the entire blades. For flat blades, which we shall consider here, the upwash on the jth blade induced by its motion is spatially linear:

$$\begin{aligned}\tilde{W}_j^{(m)}(\xi,\tau) &= \frac{W_j^{(m)}(\xi,\tau)}{U} = -\frac{\beta_j}{\tilde{U}}\tilde{h}'_j + \alpha_j + \frac{\beta_j}{\tilde{U}}(\xi - \xi_{ea})\alpha'_j \\ &= \left(-\frac{\beta_j}{\tilde{U}}\tilde{h}'_j + \alpha_j - \frac{\xi ea_j\beta_j}{\tilde{U}}\alpha'_j\right) + \xi\left(\frac{\beta_j}{\tilde{U}}\alpha'_j\right) \\ &= \tilde{W}_{U_j}(\tau) + \xi\ \tilde{W}_{R_j}(\tau). \end{aligned} \tag{3}$$

In the last equalities, we decompose the upwash into spatially Uniform (U) and spatially Ramp-like (R) components. Therefore, to model the "circulatory" part of the lift on one of the blades, we employ four Duhamel integrals:

$$\begin{aligned}\tilde{L}_j^{(C)} = &\int_{-\infty}^{\tau} \Phi^L_{U_{j1}}\left(\tilde{U}(\tau-\tau_0)\right)\frac{\mathrm{d}\tilde{W}_{U_1}}{\mathrm{d}\tau_0}\,\mathrm{d}\tau_0 + \int_{-\infty}^{\tau} \Phi^L_{U_{j2}}\left(\tilde{U}(\tau-\tau_0)\right)\frac{\mathrm{d}\tilde{W}_{U_2}}{\mathrm{d}\tau_0}\,\mathrm{d}\tau_0 \\ &+ \int_{-\infty}^{\tau} \Phi^L_{R_{j1}}\left(\tilde{U}(\tau-\tau_0)\right)\frac{\mathrm{d}\tilde{W}_{R_1}}{\mathrm{d}\tau_0}\,\mathrm{d}\tau_0 + \int_{-\infty}^{\tau} \Phi^L_{R_{j2}}\left(\tilde{U}(\tau-\tau_0)\right)\frac{\mathrm{d}\tilde{W}_{R_2}}{\mathrm{d}\tau_0}\,\mathrm{d}\tau_0, \end{aligned} \tag{4}$$

which incorporate the uniform and ramp-like upwash inputs of both blades. The analogues, Φ^L_*, to Wagner's function are step responses to the four inputs: $\tilde{W}_{U_1}$, $\tilde{W}_{U_2}$, $\tilde{W}_{R_1}$, $\tilde{W}_{R_2}$. The reader is referred to Coller and Chamara (2004) for an explanation of the scaling $\tilde{U}$ within the step response functions.

To incorporate these effects into a low-order model, we represent the step response functions as finite sums of exponentials:

$$\Phi^{(L)}_*(\tau) \approx \phi^{(L)}_{*\infty}\left(1 - \sum_{m=1}^{N^{(L)}_*} K^{(L)}_{*m} \mathrm{e}^{\sigma^{(L)}_{*m}\tau}\right). \tag{5}$$

As outlined in Coller and Chamara (2004), this allows us to re-express the integral

$$\int_{-\infty}^{\tau} \Phi^{(L)}_*(\tau-\tau_0)\frac{\mathrm{d}\tilde{W}_*}{\mathrm{d}\tau_0}\,\mathrm{d}\tau_0 \approx G^{(L)}_{*0}(\tau) + G^{(L)}_{*1}(\tau) + \cdots + G^{(L)}_{*N^L_*}(\tau), \tag{6}$$

where

$$G^{(L)}_{*0}(\tau) = \phi^{(L)}_{*\infty}\left(1 - \sum_{m=1}^{N^{(L)}_*} K^{(L)}_{*m}\right)\tilde{W}_*(\tau)$$

and

$$G^{(L)}_{*j}(\tau) = \sigma^{(L)}_{*j}\tilde{U}(G^{(L)}_{*j}(\tau) - \phi^{(L)}_{*\infty}K^{(L)}_{*j}\tilde{W}_*(\tau)) \quad \text{for } j > 0.$$

Thus, the "circulatory" parts of the system are expressed as a combination of simple linear ordinary differential equations.

Since the "memoryless" terms tend to represent apparent mass effects proportional to blade acceleration, we express them in terms of time derivatives of upwash inputs:

$$\tilde{L}_j^{(M)} = \frac{C^{(L)}_{U_{j1}}}{\tilde{U}}\tilde{W}'_{U_1} + \frac{C^{(L)}_{U_{j2}}}{\tilde{U}}\tilde{W}'_{U_2} + \frac{C^{(L)}_{R_{j1}}}{\tilde{U}}\tilde{W}'_{R_1} + \frac{C^{(L)}_{R_{j2}}}{\tilde{U}}\tilde{W}'_{R_2}. \tag{7}$$

Observe that upon differentiating expressions for the uniform and ramp-like upwashes in Eq. (3) and substituting into Eq. (7), the memoryless terms take the same form and scaling as that of the single airfoils (Coller and Chamara, 2004). This feature is important since, as $\tilde{d}\to\infty$, the two airfoil system becomes equivalent to two isolated airfoils.

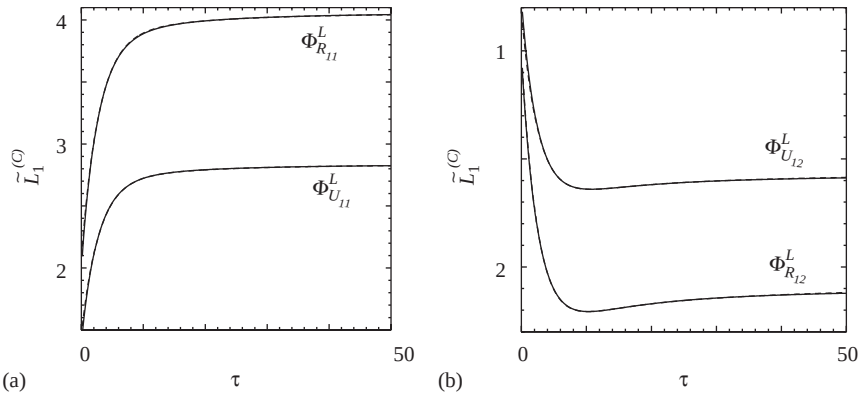

Fig. 2. Step responses for the lift due to the presence of uniform and ramp-like upwashes on each of the blades. While the responses due to low-order model are dashed and those of the high fidelity simulation are solid, the curves lie almost directly on top of each other and cannot be distinguished.

Coefficients K, σ, $\phi_{*\infty}$ are obtained by fitting the step responses of the model to those of high fidelity vortex lattice simulations. The high-order simulations are straightforward extensions of single airfoil simulations outlined in Coller and Chamara (2004) which produced results nearly identical to isolated airfoil theory. Provided our previous assumptions of ideal flow and linear aerodynamic response are approximately satisfied, the simulations should produce a good representation of the physical system. Also outlined in Coller and Chamara (2004) is a procedure for fitting the aerodynamic coefficients. The coefficients we obtain are tabulated in Appendix A.

To demonstrate how well our expansions (5) coincide with the true step responses, we show four typical cases in Fig. 2. The step response curves due to the low-order model are dashed while those of the high fidelity simulation are solid. It is difficult to distinguish them in the figure since they lie almost directly on top of each other.

The coefficients for the memoryless terms in Eq. (7) are determined by running the high fidelity simulation with the input upwash modes individually varying sinusoidally in time. After subtracting the circulatory part of the lift from the numerical lift data, it is a simple matter to fit the parameters. The procedure yields the same coefficients regardless of the chosen forcing frequency.

In an identical manner, the aerodynamic moment can be modelled by linear, first-order ODEs that capture "circulatory" effects and linear combinations of accelerations representing "memoryless" effects. The coefficients and exponents for the moment are also tabulated in Appendix A. They correspond to moments about the leading edge (*le*) of the airfoil. To convert to a moment about the elastic axis (*ea*) as required by (1), one must perform the translation $\tilde{M}_{ea_j} = \tilde{M}_{le_j} + \xi_{ea_j}\tilde{L}_j$.

Upon substitution of the aerodynamic forces into the equations of motion (1), the system reaches closure. In state space form, we express the equations generally as

$$\boldsymbol{x}' = \boldsymbol{B}\boldsymbol{x} + \boldsymbol{F}(\boldsymbol{x}). \tag{8}$$

The vector x contains eight mechanical states plus 38 fluid states, $G^{\#}_{*j}$. The quantity $F(x)$ contains the structural nonlinearities.

2.1. Flutter boundaries and existence of Hopf–Hopf bifurcations

For the fixed parameters listed in the caption, the shaded region in Fig. 3 corresponds to values of X_2 and $\tilde{U}$ for which the reduced-order model is locally stable. The circular symbols in the figure depict values of parameters for which our high fidelity vortex lattice simulations predict a stability boundary. We see good agreement between the model and simulation. These data are the same as that presented in Chamara and Coller (2000).

New data presented in the plot are the curves S_0 and S_1. One curve coincides with points in (X_2, $\tilde{U}$) space on which one complex conjugate pair of eigenvalues is purely imaginary. The other curve coincides with another purely imaginary pair of eigenvalues. Both curves constitute part of the flutter boundary. At locations where S_0 and S_1 intersect, two oscillatory modes go unstable simultaneously and the system exhibits Hopf–Hopf instabilities.

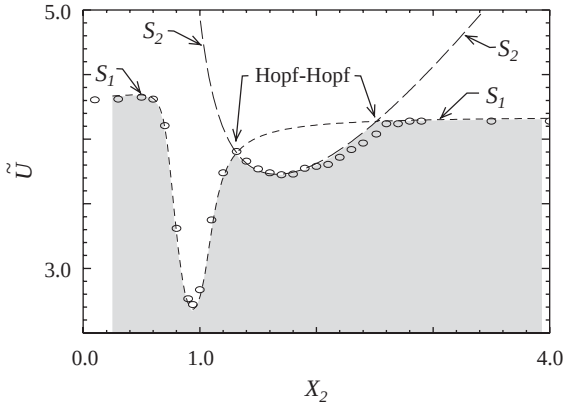

Fig. 3. Criticality curves and flutter boundary predicted by reduced-order model. For comparison, circles are points on flutter boundary as computed by high fidelity simulation. Parameters held fixed are $\chi_1 = 0.1$, $X_1 = 2$, $\mu_1 = 20$, $\xi_{ea_1} = 0.5$, $r_{\alpha_1} = 0.5$, $\chi_2 = 0.2$, $\mu_2 = 20$, $\xi_{ea_2} = 0.1$, $r_{\alpha_2} = 0.5$, $Y_2 = 2.0$, $\tilde{d} = 0.5$, $\beta_2 = 1$.

3. Abundance of Hopf–Hopf instabilities

One of the issues left unresolved in our previous study is the degree to which double flutter is "prevalent" in the two-airfoil systems. Before loosely defining what we mean by "prevalent," we first note that S_0 and S_1 are each co-dimension one. That is, in an n dimensional parameter space, the sets occupy a surfaces of dimension $n-1$. As illustrated schematically in Fig. 4(a), the set of double Hopf bifurcations occur on $S_0 \cap S_1$ and thus lie on a surface of dimension $n-2$, co-dimension two. As one varies parameters continuously, therefore, it is with probability zero that one passes directly through a Hopf–Hopf instability. When asking whether double flutter is "prevalent," though, we are asking whether the Hopf–Hopf curves are interwoven throughout parameter space like the ubiquitous "strings" in a stalk of celery, or whether instances in slices of parameter space such as that shown in Fig. 3 rare.

For $r_{\alpha_1} = r_{\alpha_2} = 0.5$, $\xi_{ea_j} = 0.5$, $\chi_j = 0.2$, $\mu_j = 20.0$, $\beta_2 = 1$, $\tilde{d} = 0.5$, and Y_2 taking on several values between 1.0 and 0.5, we plot values of frequency ratios X_1 and X_2 in Fig. 5 for which double Hopf instabilities reside on the flutter boundary. The curves in Fig. 5 represent projections of the intersections $S_0 \cap S_1$, as indicated in Fig. 4, which lie on the flutter boundary.

At the beginning of the sequence (Fig. 5(a)), the two airfoils are identical, and thus the curves are reflection symmetric about the line $X_1 = X_2$. However, upon perturbing Y_2 from 1.0, we break the symmetry. Fig. 5(b) shows branches 1 and 3 approaching each other as Y_2 is reduced slightly. Between $Y_2 = 0.96$ and 0.83, branches 1 and 3 each split. Sub-branches 1a and 3a then merge as depicted in Figs. 5(b) and (c). The entire sequence in Fig. 5 shows several such mergings and splittings, including the genesis of branch 4 between $Y_2 = 0.57$ and 0.54. The geometric interpretation of the Hopf–Hopf curves in Fig. 4 as the intersection of criticality surfaces allows for straightforward explanation of most splittings and mergings. However, an explanation of the gaps and branch terminations requires closer examination.

In Fig. 6, we plot criticality surfaces S_j to explain the termination of branches 1b and 1a in Fig. 5(c). Three slices through the parameter space at $X_1 = 0.8$, 0.64, and 0.6 are investigated; the S_0 curve has short dashes while S_1 has long dashes. Starting the discussion with slice (c), note that S_0 and S_1 intersect at three locations. The intersections are labelled according to their branch numbers in Fig. 5(c).

At $X_1 = 0.64$, shown in Fig. 6(b), all three intersections of S_0 and S_1 still exist. However, for low values of X_2, the plot clearly shows that S_1 clearly folds back upon itself. As a consequence, the flutter boundary exhibits a discontinuous jump. It is a standard cusp catastrophe (Poston and Stewart, 1978). Because of this, the intersection no longer lies on the flutter boundary and branch 1a in Fig. 5(c) terminates.

The transition from $X_1 = 0.64$ to 0.6 is even more dramatic. On branch 1b, the two pairs of eigenvalues approach each other and then coalesce at the branch's left-most termination point. It is similar to a Hamiltonian Hopf. As the eigenvalues merge, some of the lobes of S_0 and S_1 switch places, detangling the previous intersection. As a result, branch 1b in Fig. 5(c) terminates. The apparent kink in the flutter boundary of slice (a) is a remnant of the previous Hopf–Hopf instability, and gets smoothed out as one moves away from the termination point.

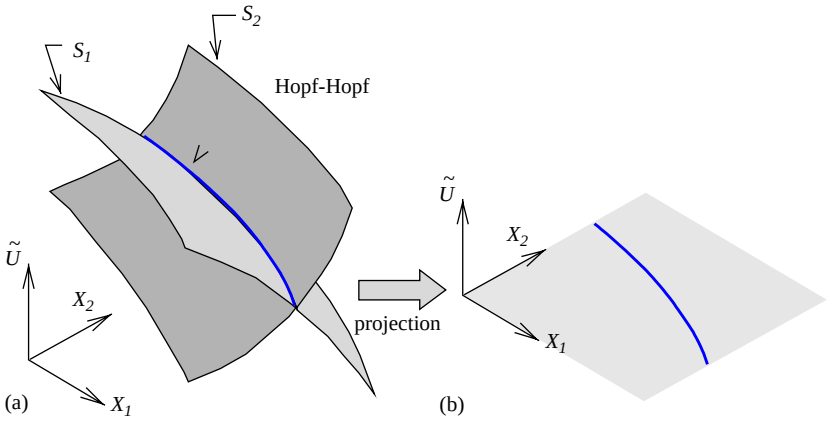

Fig. 4. (a) Hopf–Hopf bifurcations lie at the intersection of criticality surfaces S_0 and S_1. (b) Simple projection of Hopf–Hopf curve onto (X_1, X_2) space.

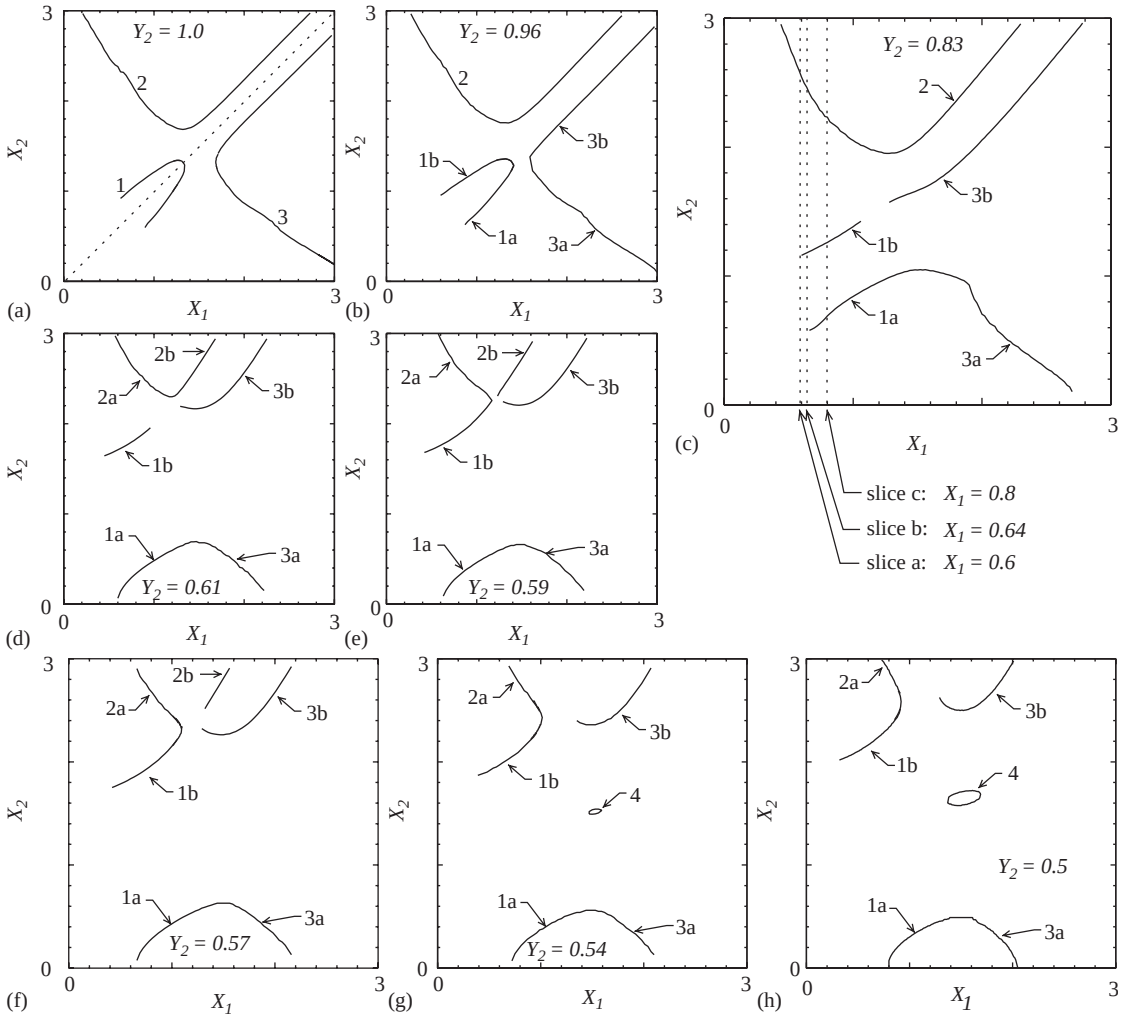

Fig. 5. Root locus of Hopf–Hopf instabilities as Y_2 varies from 1.0 to 0.5.

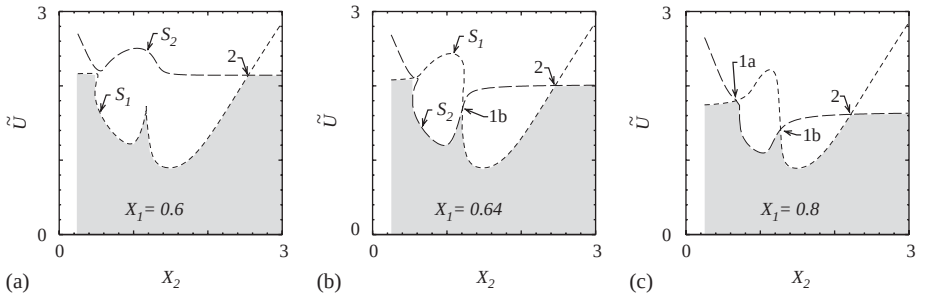

Fig. 6. Plots of critically curves from three slices of parameter space in Fig. 5c.

These two instances are typical of the mechanisms that cause Hopf–Hopf branches in Fig. 5 to suddenly terminate. We find that co-dimension 2 slices of the parameter space such as shown in Fig. 5 often do show Hopf–Hopf branches. Although not as dense as "strings" in a celery stalk, the double Hopf instabilities prevail in the two airfoil system.

4. Dynamical system with structural nonlinearities

Our next task is to study the nonlinear aspects of the two interacting aeroelastic instabilities. Dynamical systems theory provides a set of tools than can be applied to the specific set of model Eqs. (1). However, before diving directly into nonlinear analysis of Eqs. (1), we find it enlightening to first discuss the nonlinear interaction of two nearly coincident Hopf bifurcations in a general setting, not specific to flutter.

4.1. Generic Hopf–Hopf phenomena

Provided mild genericity conditions hold, and that there are no low-order resonances, the "essential" dynamics of *any* system within some neighborhood of two (and only two) nearly coincident Hopf bifurcations can be transformed into the following set of differential equations (Coller and Chamara 2004; Guckenheimer and Holmes 1983):

$$\begin{aligned}\dot{a}_0 &= a_0(\lambda_0 + c_{00}a_0\bar{a}_0 + c_{01}a_1\bar{a}_1) + \mathcal{O}(5),\\ \dot{a}_1 &= a_1(\lambda_1 + c_{10}a_0\bar{a}_0 + c_{11}a_1\bar{a}_1) + \mathcal{O}(5).\end{aligned} \tag{9}$$

All inessential terms are removed, leaving only those cubic terms necessary to characterize the leading nonlinear dynamic behavior. Eqs. (9), collectively, are called the normal form of a Hopf–Hopf bifurcation. Dependent variables a_0 and a_1 above are complex; thus the relatively simple set of equations possesses a four dimensional state space. Parameters λ_j, c_{jk} are also complex and their values depend upon parameters and other details of the original system.

One particularly attractive feature of the Hopf–Hopf normal form (9) is that the equations inherit an $S^1 \times S^1$ normal form symmetry from the linear part of the flow (Elphick et al., 1987). As a consequence, when we write the dependent variables in Eq. (9) as $a_k = \rho_k \exp(\mathrm{i}\phi_k)$, the ODEs for the magnitudes ρ_k become

$$\dot{\rho}_k = \rho_k[\Re e(\lambda_k) + \Re e(c_{k0})\rho_0^2 + \Re e(c_{k1})\rho_1^2] + \mathcal{O}(\rho^5). \tag{10}$$

The important point to note here is that the amplitude equations are independent of the phases ϕ_0 and ϕ_1.

Because of the universality of the normal form and its applicability to a wide variety of problems, the dynamics of the canonical system already have been studied. [See, for example, Coller (2004), Guckenheimer and Holmes (1983).] A road map of bifurcations and dynamic phenomena has been created, and one can apply these results to new problems. To briefly outline the Hopf–Hopf normal form dynamics, we rewrite the equations once again:

$$\begin{aligned}\dot{r}_0 &= r_0(\mu_0 - r_0^2 + br_1^2),\\ \dot{r}_1 &= r_1(\mu_1 - cr_0^2 + dr_1^2).\end{aligned} \tag{11}$$

Fifth-order terms have been truncated. The dependent variables r_0 and r_1 above are scaled versions of the amplitudes ρ_0 and $\rho_1 : r_j = \rho_j\sqrt{\Re e(c_{jj})}$. Necessarily, then, the coefficient d is either $+1$ or -1. To get the coefficient of the $r_0^2 r_1$ term in the first equation of Eq. (11) to be -1, it might be necessary to reverse time. This is only for purposes of efficient taxonomy. By keeping track of a time reversal, it is a simple matter to reverse arrows on solution trajectories in the last stage of the analysis if necessary.

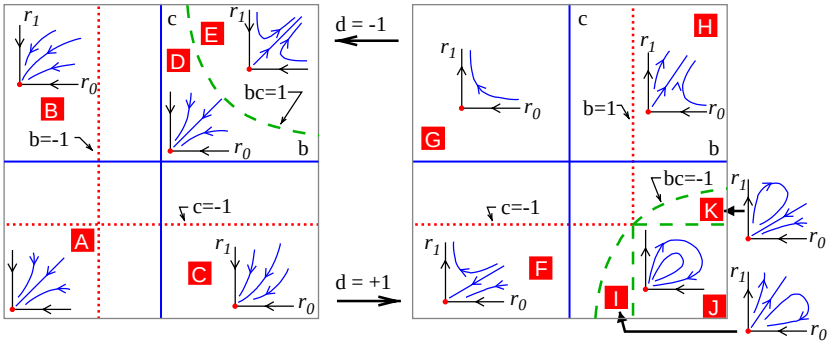

Fig. 7. Phase portraits for the doubly degenerate cases of Eq. (11) with $\mu_0 = \mu_1 = 0$.

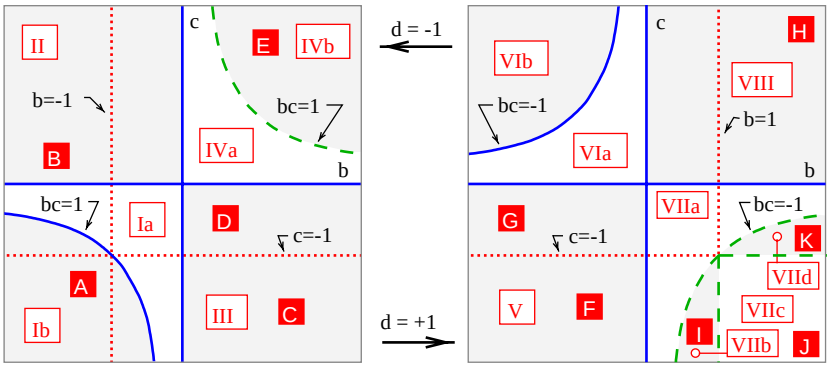

Fig. 8. Partial parameter space for Hopf–Hopf normal form (11). Dotted lines separate different degenerate behaviors (solid letters). Solid lines separate nondegenerate classes (open roman numerals). Dashed lines serve the dual purpose.

To construct the Hopf–Hopf normal form from a set of differential equations, one first chooses system parameters so that both oscillatory instabilities are critical simultaneously. Then, one performs a series of coordinate transformations that accomplishes a center manifold reduction and removes all nonlinear terms except those in Eq. (9). Because of the double criticality, the real part of both λ_0 and λ_1 are identically zero. Equivalently, $\mu_0 = \mu_1 \equiv 0$ in Eq. (11). Fig. 7 shows all possible phase portraits for the scaled normal form amplitude equations (11) corresponding to co-dimension two degeneracies $\mu_0 = \mu_1 = 0$. In all, the lines $r_0 = 0$ and $r_1 = 0$ are invariant. Therefore, the portraits lie in the positive quadrant r_0, $r_1 \geqslant 0$. We label the portraits with letters *A* through *K*. The dotted and dashed curves within the *b*, *c*, and *d* parameter space are the boundaries which separate the different types of portraits.

If we embed system parameters into the center manifold (Wiggins, 1990), then we can formally perturb the system off the double instability, and consequently perturb the normal form off of the cases with $\mu_0 = \mu_1 = 0$. When we let the linear coefficients μ_j in Eq. (11) be nonzero, there are 11 families and a handful of sub-families of phase portraits to consider. The locations of these families within the *b*, *c*, and *d* parameter space are labeled with roman numerals in Fig. 8.

The individual phase portraits for all the families are shown in Fig. 9. There are a total of 66 nondegenerate cases one obtains from Eq. (11). However, if we account for possible time reversals necessary to transform Eq. (10) to Eq. (11), we get an additional 66 portraits, identical to those shown in Fig. 9, except the sense of the arrows is reversed. While some of the portraits in Fig. 9 may appear similar to others, they occur through different sequences of bifurcations and have different neighboring behaviors. Therefore, we consider them distinct. Thus, there exists an enormous wealth of dynamic possibilities that may emerge from Hopf–Hopf instabilities.

4.2. *A hypothetical bifurcation sequence*

To illustrate how a sequence of portraits from Fig. 9 might appear in a double flutter problem, suppose that we choose parameters identical to those used to generate Fig. 3, and set X_2 just slightly greater than the double flutter value

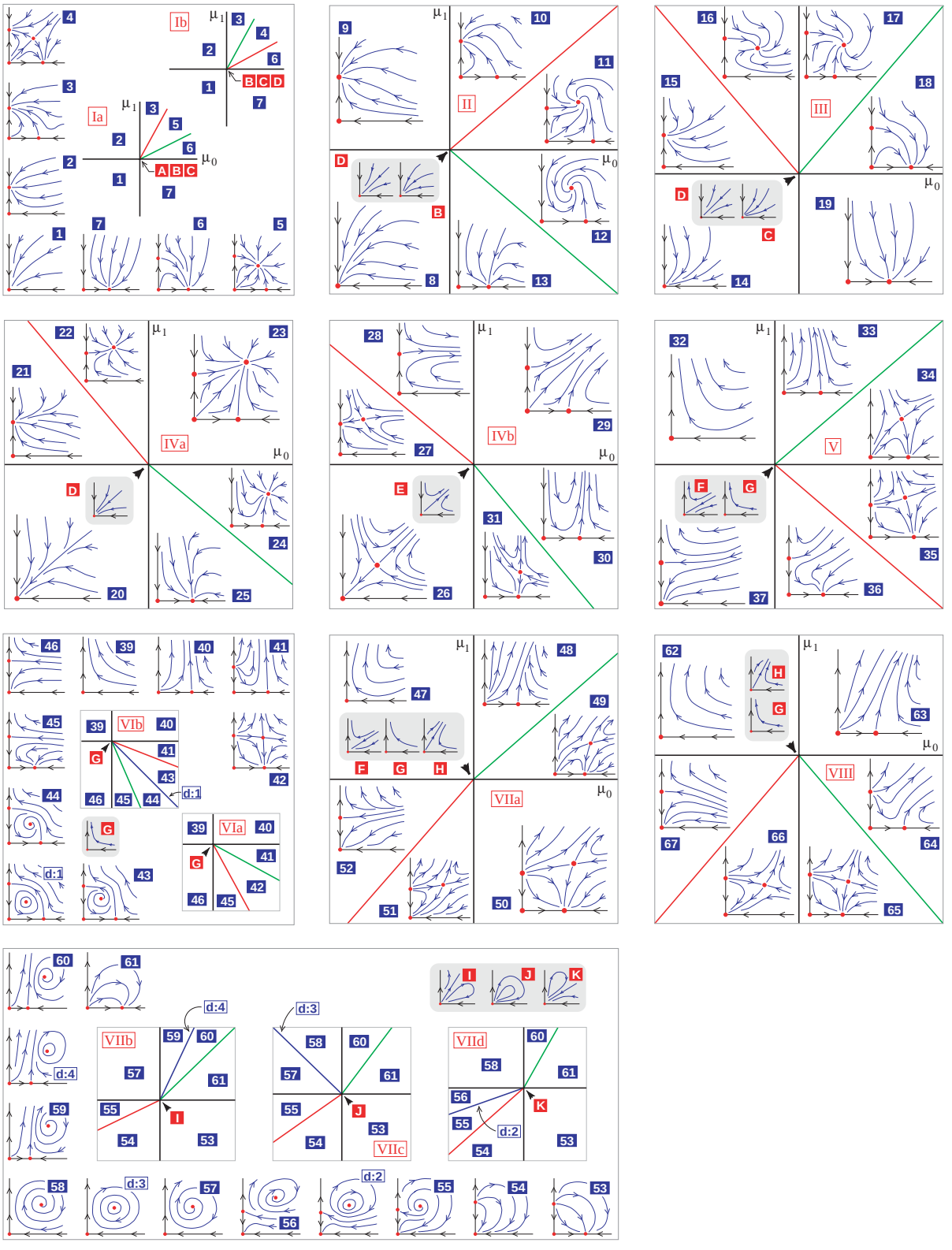

Fig. 9. Phase portraits for two interacting Hopf bifurcations. Sixty-six additional nondegenerate cases are obtained by reversing the sense of the arrows.

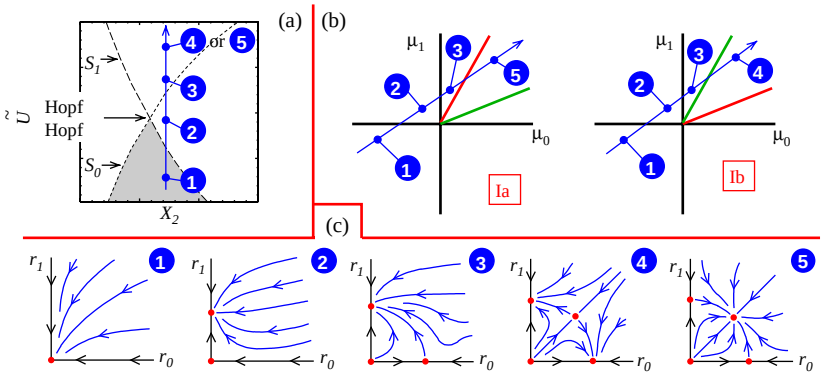

Fig. 10. A hypothetical sequence of bifurcations in the neighborhood of Hopf–Hopf. (a) $\tilde{U}$ starts from the stable regime and increases past the flutter boundary and secondary instability. (b) Assuming parameters b and c of the normal form (11) are negative, we encounter portraits of family I. (c) Portraits encountered.

of 1.315267. Fig. 10(a) zooms in on the left-most Hopf–Hopf point of Fig. 3. As we continuously increase the flow speed $\tilde{U}$, the system follows the vertical line in the figure.

Suppose further, that the structural nonlinearities of the double flutter problem are such that coefficients b and c in the scaled normal form amplitude equations (11) are negative, and $d=-1$. Therefore, the phase portraits for the double flutter system belongs to either family Ia or Ib, depending on whether $bc<1$ or $bc>1$, respectively.

If $\tilde{U}$ is chosen sufficiently small, the double flutter system is stable and the corresponding values of μ_0 and μ_1 in Eq. (11) are both negative. Therefore, regardless of whether the normal form resides in family Ia or Ib, this small value of $\tilde{U}$ leads to Portrait 1 shown in Fig. 10(c). In addition to being stable, the point $r_0=r_1=0$ is a global attractor for the cubic order normal form. When r_0 and r_1 are zero simultaneously, both oscillation amplitudes are zero, and hence the airfoils sit motionless in their undeflected states.

As we increase the flow speed $\tilde{U}$, the system crosses the criticality curve S_1. Therefore, μ_1 goes from negative to positive accordingly, and the normal form portraits switch from case 1 to case 2. In Portrait 2, the point $r_0=r_1=0$ is still an equilibrium, as it is in all portraits of Fig. 9. This time, however, the equilibrium is unstable in the r_1 direction; it undergoes a pitchfork bifurcation which gives birth to another (stable) equilibrium on the r_1-axis. We refer to this new equilibrium on the r_1-axis as a relative equilibrium since it is only an equilibrium for the amplitude equation. In Eqs. (9), or in the original state variables, it corresponds to a stable periodic orbit that results from a supercritical Hopf bifurcation.

Increasing $\tilde{U}$ still further, μ_0 becomes positive as the aeroelastic system crosses S_0. The scaled normal form amplitude equations yield Portrait 3. Another relative equilibrium appears, this one on the r_0-axis. The new equilibrium is unstable, and nearly all trajectories are still attracted to the relative equilibrium on the r_1-axis. In the full system, we would expect solutions to be attracted to a single oscillation mode.

The next bifurcation, as $\tilde{U}$ increases, depends on whether the system lies within Family Ia or Ib. If $bc<1$ (Family Ia), then the relative equilibrium on the r_1-axis loses stability, giving birth to a new equilibrium for which both r_0 and r_1 are nonzero as shown in Portrait 5. This new relative equilibrium corresponds to a two-frequency oscillation involving both marginal modes. The new mixed-mode equilibrium is locally stable and it attracts almost all solutions of (11).

If $bc>1$, then the bifurcation following Portrait 3 gives way to Portrait 4. In this case, the bifurcation alters the stability of the relative equilibrium on the r_0-axis. It gains stability as it spawns an unstable, mixed-mode, relative equilibrium of saddle type. Therefore, the relative equilibria on the r_0 and on the r_1 axes both attract nearby solutions. The mixed mode equilibrium that forms in the process is of saddle type as depicted in Portrait 4 of Fig. 10(c). Its stable manifold serves as a separatrix which divides the amplitude space into regions for which solutions get attracted to one single-mode relative equilibrium or the other.

Other potential bifurcation sequences in Fig. 9 can be traced in a similar manner.

4.3. Analysis of the aeroelastic system

Our next task is to determine which of the phase portraits actually appear in the two-airfoil aeroelastic system. Given that there are 132 possibilities in the generic cubic order Hopf–Hopf bifurcation, it would be interesting to investigate how many of these occur.

4.3.1. Transformations

To answer these questions, we must transform the equations of motion (1) into normal form. The procedure is outlined in Coller and Chamara (2004) in the context of a single blade flutter problem. A more general theoretical discussion may be found in Guckenheimer and Holmes (1983).

The first step is to decompose and linearly transform the state equations (8) into the form

$$\boldsymbol{x}_c' = B_c\boldsymbol{x}_c + \boldsymbol{f}(\boldsymbol{x}_c, \boldsymbol{x}_s), \tag{12}$$

$$\boldsymbol{x}_s' = B_s\boldsymbol{x}_s + \boldsymbol{g}(\boldsymbol{x}_c, \boldsymbol{x}_s). \tag{13}$$

The symbol x_s denotes the states that lie in the stable eigenspace. Therefore, the eigenvalues of B_s all have negative real parts.

Meanwhile, the matrix B_c takes the form

$$B_c = \begin{bmatrix} 0 & -\omega_0 & 0 & 0 & 0 & \cdots & 0 \\ \omega_0 & 0 & 0 & 0 & 0 & \cdots & 0 \\ 0 & 0 & 0 & -\omega_1 & 0 & \cdots & 0 \\ 0 & 0 & \omega_1 & 0 & 0 & \cdots & 0 \\ 0 & 0 & 0 & 0 & 0 & \cdots & 0 \\ \vdots & \vdots & \vdots & \vdots & \vdots & \ddots & \vdots \\ 0 & 0 & 0 & 0 & 0 & \cdots & 0 \end{bmatrix} \quad \text{and} \quad \boldsymbol{f}(\boldsymbol{x}_c, \boldsymbol{x}_s) = \begin{bmatrix} f_{0r}(\boldsymbol{x}_c, \boldsymbol{x}_s) \\ f_{0i}(\boldsymbol{x}_c, \boldsymbol{x}_s) \\ f_{1r}(\boldsymbol{x}_c, \boldsymbol{x}_s) \\ f_{1i}(\boldsymbol{x}_c, \boldsymbol{x}_s) \\ 0 \\ \vdots \\ 0 \end{bmatrix}.$$

The first four elements of x_c are the states on the center eigenspace. The remaining elements of x_c are bifurcation parameters that have been embedded in the center eigenspace as described in Wiggins (1990).

Separating the stable and marginally stable parts of the system allows us to apply the center manifold theorem (Guckenheimer and Holmes, 1983), and thus we may express the stable states explicitly in terms of center states: $x_s = h(x_c)$. Substituting the center manifold expression into the first four equations of Eq. (12), and expressing them in complex form ($z_0 = x_{c_1} + \mathrm{i}x_{c_2}, z_1 = x_{c_3} + \mathrm{i}x_{c_4}$), we arrive at equations of the form

$$\begin{aligned} \dot{z}_0 &= \lambda_0 z_0 + f_0(z_0, \bar{z}_0, z_1, \bar{z}_1), \\ \dot{z}_1 &= \lambda_1 z_1 + f_1(z_0, \bar{z}_0, z_1, \bar{z}_1), \end{aligned} \tag{14}$$

which represent the dynamics of the system on the four-dimensional center manifold.

Finally, to transform Eq. (14) into normal form (9), it is straightforward to apply the formulae from Coller (2004), reproduced in Appendix B. Therefore, for a given system, or family of systems, it is possible to make the transformations and then "look up" the corresponding qualitative phase portraits from Figs. 8 and 9.

4.3.2. Abundance of possibilities

To answer the second question posed at the beginning of Section 4.3, how many of the generic Hopf–Hopf phenomena exist in the two-airfoil problem, we consider a physical system with only cubic nonlinearities. As outlined in Section 4.1, we start with system parameters such that the system possesses a co-dimension two double Hopf instability. As demonstrated in Coller and Chamara (2004), the center manifold in such cases plays no role in the cubic order normal form. Eq. (14) is obtained via simple linear transformation. The nonlinear parts, f_0 and f_1, are cubic in z_j, $\bar{z}_j$. Therefore, the normal form coefficients in Eq. (9) are particularly simple to calculate:

$$\begin{aligned} c_{00} &= \frac{1}{2}\frac{\partial^3 f_0}{\partial z_0^2 \partial \bar{z}_0}\bigg|_0, \quad c_{01} = \frac{\partial^3 f_0}{\partial z_0\, \partial z_1\, \partial \bar{z}_1}\bigg|_0, \\ c_{10} &= \frac{\partial^3 f_1}{\partial z_0\, \partial \bar{z}_0\, \partial z_1}\bigg|_0, \quad c_{11} = \frac{1}{2}\frac{\partial^3 f_1}{\partial z_1^2 \partial \bar{z}_1}\bigg|_0. \end{aligned} \tag{15}$$

The right-hand sides of the expressions in Eq. (15) are linear combinations of the structural coefficients $\delta_{h_1}3$, $\delta_{\alpha_1}3$, $\delta_{h_2}3$, and $\delta_{\alpha_2}3$, and we denote by M the linear mapping $M : (\delta_{h_1}3, \delta_{\alpha_1}3, \delta_{h_2}3, \delta_{\alpha_2}3) \mapsto (c_{00}, c_{01}, c_{10}, c_{11})$. In the absence of any degeneracies in Eq. (15), M will be invertible. Therefore, it is possible to choose the structural coefficients to achieve any combination of cubic normal form coefficients and hence achieve any combination of the coefficients b, c, and d in Eq. (11). Therefore, all eleven families and sub-families of phase portraits enumerated in Fig. 8 are possible.

By perturbing system parameters such as $\tilde{U}, Y_2, \mu_j, \xi_{ea_j}, X_j$, and r_{α_j} that directly affect the linearization, it is possible to independently perturb the coefficients μ_0 and μ_1 in Eq. (11) while altering coefficients b, c, and d only

slightly. Therefore, we conclude that *all 132 nondegenerate cases of Fig. 9 are generically possible* in a Hopf–Hopf, double flutter interaction.

Furthermore, we note that the quadratic structural coefficients, $\delta_{h_1 2}, \delta_{\alpha_1 2}, \delta_{h_2 2}, \delta_{\alpha_2 2}$, provide additional freedom in the choice of normal form coefficients b, c, and d. Therefore, to achieve a desired case, the extra freedom might allow for more practical choices of system parameters.

4.4. Numerical comparisons

To verify that the normal form analysis correctly predicts the dynamics the physical system, we consider in more detail the double Hopf instability discussed hypothetically in Section 4.2. At the left-most double Hopf instability in Fig. 3 ($X_2 = 1.315267$), the frequencies associated with the two critical modes are 1.95 and 2.96. Therefore, there are no frequency resonances below fifth order and the normal form is that presented in Eq. (9). Furthermore, the bifurcation is not degenerate so the neighboring systems are capable of exhibiting all 132 Hopf–Hopf interactions. In fact, the hypothetical sequences outlined in Section 4.2 are possible.

4.4.1. Generating portrait 5

In the first two numerical examples, we choose parameters for which the normal form analysis predicts the more interesting cases from Fig. 10. Our normal form analysis predicts that, for parameters listed in the caption of Fig. 11, the system exhibits the phenomena of Portrait 5. It is a case for which the only attracting solution is the mixed-mode relative equilibrium corresponding to a combination of two oscillations. Fig. 11(a) shows time traces of plunge of one of the blades, computed from numerical simulations of the reduced-order model equations. In agreement with the phase portrait, a small initial condition initially grows; then, the oscillation amplitude plateaus. Since the growth rate is much slower than the time scale of the oscillations, it is difficult to discern the wave form of the plot. However, we also show

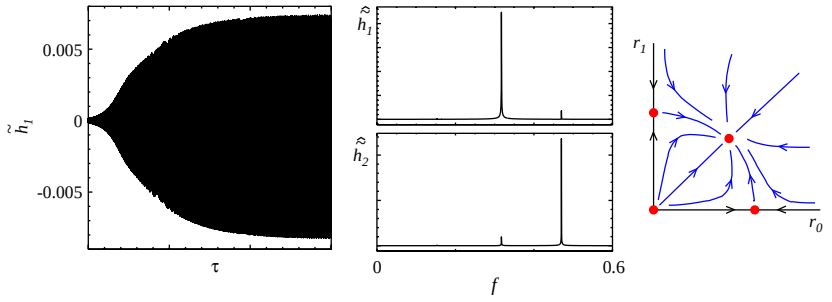

Fig. 11. Time trace of $\bar{h}_1$ and Fourier spectra of $\tilde{h}_1$ and $\tilde{h}_2$ computed using reduced-order model. Dynamic behavior is that of Portrait 5. Parameters are the same as those used in Fig. 3 except $\chi_1 = 0.101$, $\chi_2 = 0.199$, $X_2 = 1.315267$, $\tilde{U} = 3.89436$, $\delta_{\alpha_1 2} = 20.0$, $\delta_{h_1 2} = 20.0$, $\delta_{\alpha_2 2} = 20.0$, $\delta_{h_2 2} = 20.0$, $\delta_{\alpha_1 3} = 600.0$, $\delta_{h_1 3} = 1444.9$, $\delta_{\alpha_2 3} = 600.0$, $\delta_{h_2 3} = 176.0$.

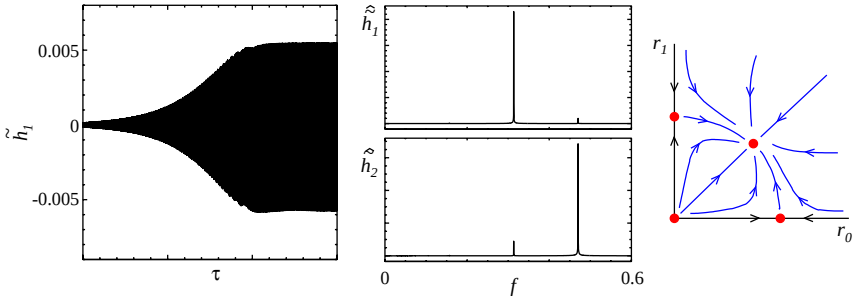

Fig. 12. Time trace of $\tilde{h}_1$ and Fourier spectra of $\tilde{h}_1$ and $\tilde{h}_2$ computed using high fidelity vortex lattice simulation. Dynamic behavior is that of Portrait 5. Parameters are the same as those used in Fig. 11.

Fourier transforms of the $\tilde{h}_1$ and $\tilde{h}_2$ signals in the figure. They clearly indicate the presence of two incommensurate dominant harmonics, consistent with the stable mixed-mode relative equilibrium in the phase portrait.

To demonstrate that the Portrait 5 behavior in Fig. 11 is not an artifact of our modeling assumptions, we show time traces and Fourier spectra generated from a high fidelity vortex lattice simulation in Fig. 12. Parameter values are the same as those used to generate Fig. 11. It is clear that the reduced-order model and high fidelity simulation agree and they both exhibit phenomena of Portrait 5 as predicted by the normal form analysis.

4.4.2. Generating portrait 4

In our second numerical example, we choose system parameters for which the normal form predicts Portrait 4. Fig. 13 shows time traces and spectra for the new system whose parameters are listed in the caption. As discussed in Section 4.2, the case posses a mixed-mode relative equilibrium of saddle type and two locally stable, single-mode, relative equilibria. The stable manifold of the saddle serves as a separatrix. In Fig. 13, we show time traces and spectra corresponding to initial conditions lying on opposite sides of the separatrix. In part (a), the initial condition sits just below the separatrix. As indicated in the accompanying phase portrait, the corresponding solution approaches the mixed mode equilibrium and then turns toward the single-frequency, stable, relative equilibrium on the r_0-axis. The initial condition in Fig. 13(b) lies just above the separatrix. Its corresponding solution approaches the mixed mode equilibrium and then turns toward the stable, single-frequency equilibrium on the r_1-axis. The Fourier transforms show that there is only one base harmonic in each of the figures, and the frequencies differ.

As before, in Fig. 14 we present similar results from high fidelity vortex lattice simulations. Results demonstrate that theoretical predictions capture the behavior of the full system. Also, the comparison provides further validation of the modeling effort described previously.

4.4.3. Interesting three-frequency phenomena

Before presenting the final numerical example, we note that mixed-mode equilibria occur in many of the portraits of Fig. 9. In particular, we note instances (i.e., Portrait 44–43, Portrait 60–59, Portrait 58–57, and Portrait 56–55) in which the mixed mode equilibrium changes from a spiral sink to a spiral source. These are instances of tertiary Hopf bifurcation. They are neither subcritical nor supercritical in the cubic order normal form, since it is Hamiltonian at criticality (Cases d:1, d:4, d:3, and d:2, respectively) (Guckenheimer and Holmes, 1983). However, the cubic order

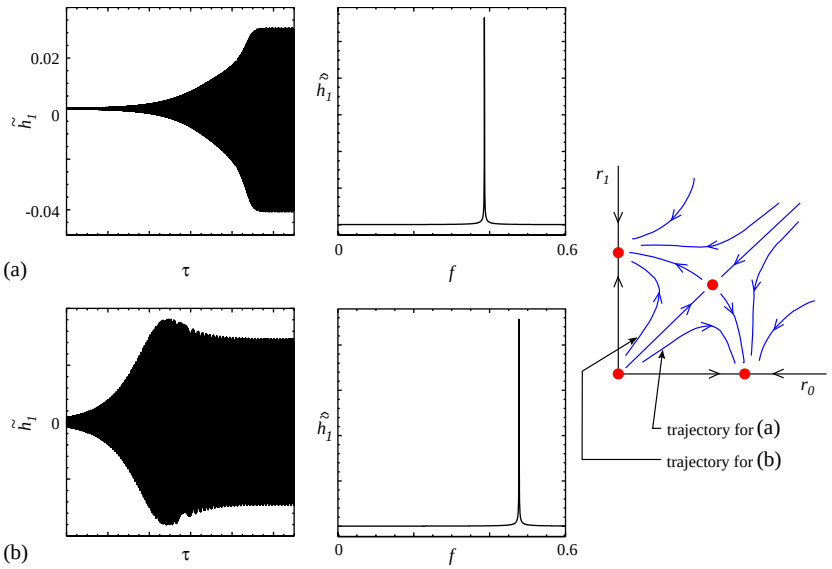

Fig. 13. Time trace and Fourier spectra for two separate initial conditions, computed using reduced-order model. Dynamic behavior is that of Portrait 4. Parameters are the same as those used in Fig. 11 except $\delta_{\alpha_1 2} = 15.0$, $\delta_{h_1 2} = 15.0$, $\delta_{\alpha_2 2} = 15.0$, $\delta_{h_2 2} = 15.0$, $\delta_{\alpha_1 3} = 600.0$, $\delta_{h_1 3} = 629.5$, $\delta_{\alpha_2 3} = 600.0$, $\delta_{h_2 3} = 1685.5$.

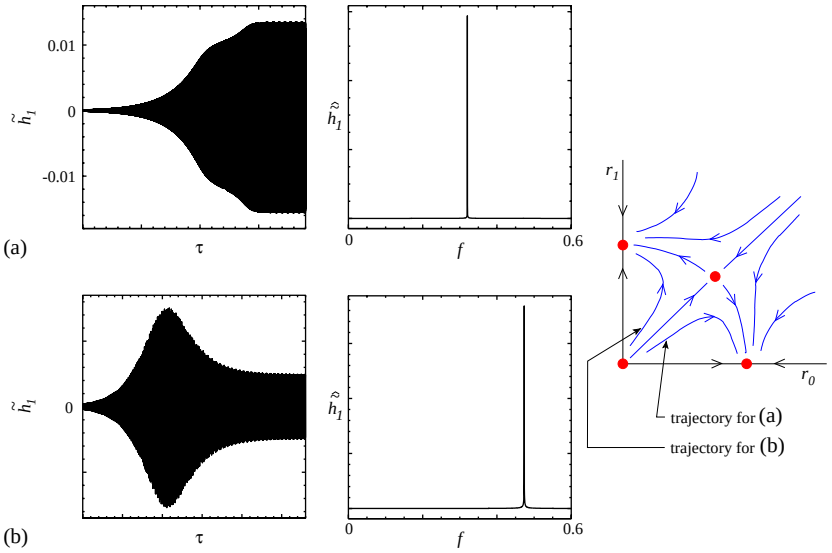

Fig. 14. Time trace and Fourier spectra for two separate initial conditions, computed using high fidelity simulation. Dynamic behaviour is that of Portrait 4. Parameters are the same as those used in Fig. 13.

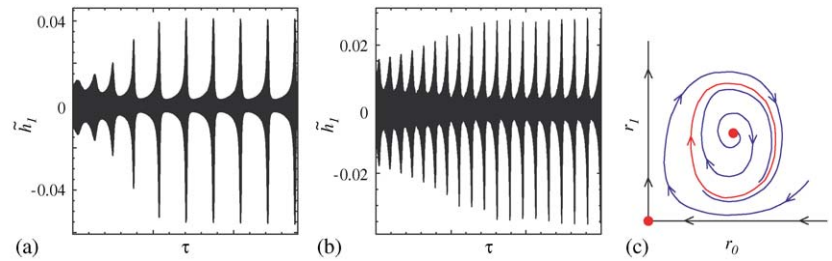

Fig. 15. (a) Three-frequency oscillation with modulating amplitude computed with reduced-order model. Parameters are the same as those used in Fig. 11 except $\chi_1 = 0.10001$, $\chi_2 = 0.20003$, $\delta_{\alpha_1 2} = 10.0$, $\delta_{h_1 2} = 10.0$, $\delta_{\alpha_2 2} = 10.0$, $\delta_{h_2 2} = 10.0$, $\delta_{\alpha_1 3} = 100.0$, $\delta_{h_1 3} = 100.1$, $\delta_{\alpha_2 3} = 90.0$, $\delta_{h_2 3} = 218.35$. (b) Analogous plot except for high fidelity simulation. Parameters are the same except $\chi_1 = 0.10015$, $\chi_2 = 0.20006$.

normal form is obtained by truncation. In general, the discarded quintic terms would cause the tertiary Hopf bifurcation to be either subcritical or supercritical.

As stated before, the mixed-mode equilibrium is associated with two oscillations and generally two incommensurate frequencies. If the tertiary Hopf bifurcation happens to be supercritical, then there are parameters for which there exists a stable limit cycle within the (r_0, r_1) amplitude space as shown on the right side of Fig. 15. It is a dynamic mechanism through which one gets a third oscillation and observes a third base frequency in the physical system.

For our third numerical example, we went hunting for such a case and found a family of them within a thin wedge of Portrait 57 in Family VIIc. Other such wedges probably exist; we did not search for them. In Fig. 15(a), we plot the time trace of one of the plunge variables for the reduced-order model. Fig. 15(b) shows an analogous plot from the high fidelity simulation. The most notable feature is the relatively slow modulation in oscillation amplitude. This is precisely the effect of the limit cycle in the phase portrait of Fig. 15.

Because the region in which the three-frequency behavior occurs is narrow, the parameters which produced the phenomenon in the high fidelity simulation are slightly different than those used in integrating the reduced-order model. Using a simple trial and error procedure, guided by the qualitative road map provided by the bifurcation diagram, it was simple to find.

5. Conclusions

The goals outlined in the Introduction have been accomplished. We have demonstrated that Hopf–Hopf interactions in the double flutter problem are abundant. Moreover, they are dynamically rich, typically exhibiting all 132 generic phenomena of the cubic order normal form.

The reduced-order modeling effort outlined herein has, once again, demonstrated its utility. The models we derive possess an important feature that makes center-manifold/normal-form analysis possible. As required by the analytical techniques, only that part of the spectrum (four eigenvalues) directly involved with the Hopf–Hopf interaction can lie near the imaginary axis. The rest of the spectrum must be safely separated. We remark that many vortex lattice-based eigenmode approaches (Hall, 1994) or other approaches based on Eulerian fluid modes (Hall et al., 2000) do not possess this property. Modes in these approaches mostly resolve fluid variables: vorticity that gets carried downstream without decay. Thus, such modeling approaches yield a dense eigenvalue spectrum near the imaginary axis.

Continuing the research presented here, we are now investigating the possibility of exploiting the rich nonlinear double flutter phenomena as the primary mechanisms for designing semi-passive flow actuators. This work is also the stepping stone for studying the largely unexplored nonlinear nature of cascade flutter in which multiple modes typically go unstable at roughly the same time. We expect the dynamic behavior there to be at least as rich.

Appendix A. Step response coefficients

Tabulated in Table 1 are the coefficients that go into the empirical step response functions in Eq. (5) and analogous responses for the moment about the leading edge. The situation corresponds to identical airfoils ($\beta_2 = 1$), and zero stagger. Dimensionless blade spacing is $\tilde{d} = 0.5$. Because of symmetry of the problem, $\Phi^{\#}_{*_{11}} = \Phi^{\#}_{*_{22}}$, and $\Phi^{\#}_{*_{12}} = \Phi^{\#}_{*_{21}}$.

Other step responses are expressed as

$$\begin{aligned}
\Phi^{L}_{R_{11}} &= 1.4418\Phi^{L}_{U_{11}} - 0.0317,\\
\Phi^{M}_{U_{11}} &= -0.5745\Phi^{L}_{U_{11}} + 0.0133,\\
\Phi^{M}_{R_{11}} &= -0.8064\Phi^{L}_{U_{11}} - 0.5572.
\end{aligned} \tag{A.1}$$

Appendix B. Formulae for normal form coefficients

Rewriting Eq. (14) as

$$\begin{aligned}
\dot{z}_0 &= \lambda_0 z_0 + p^{(0)}(z_0, \bar{z}_0, z_1, \bar{z}_1),\\
\dot{z}_1 &= \lambda_1 z_1 + p^{(1)}(z_0, \bar{z}_0, z_1, \bar{z}_1),
\end{aligned}$$

Table 1
Coefficients for step response functions in Eq. (5)

Case	$\phi^{\#}_{*\infty}$	$K^{\#}_{*i}$	$\sigma^{\#}_{*i}$
$\Phi^{(L)}_{U_{11}}$	2.844	0.429, 0.05, 0.0061	−0.36, −0.0674, −0.00344
$\Phi^{(L)}_{U_{12}}$	−1.568	0.6533, −0.1225, −0.05268	−0.366, −0.1627, −0.03168
$\Phi^{(L)}_{R_{12}}$	−2.091	−0.044, 0.684, −0.1, −0.062	−233.6, −0.397, −0.149, −0.0316
$\Phi^{(M)}_{U_{12}}$	1.045	−0.03603, 0.5763, −0.0527	−1.3465, −0.42392, −0.43297
$\Phi^{(M)}_{R_{12}}$	1.5685	−0.1417, 0.6316, −0.05026	−0.7977, −0.465−0.03945

the normal form coefficients are then given by

$$
\begin{aligned}
c_{00} =& \frac{p^{(0)}_{2100}}{2} - \frac{p^{(0)}_{0101}\bar{p}^{(1)}_{0200}}{2\bar{\lambda}_1 - 4\lambda_0} - \frac{p^{(0)}_{1010}p^{(1)}_{1100}}{\lambda_1 - \lambda_0 - \bar{\lambda}_0} + \frac{p^{(0)}_{1100}p^{(0)}_{2000}}{2\lambda_0} + \frac{p^{(0)}_{1100}\bar{p}^{(0)}_{1100}}{\lambda_0} \\
&+ \frac{p^{(0)}_{2000}\bar{p}^{(0)}_{1100}}{\bar{\lambda}_0} - \frac{p^{(0)}_{1001}\bar{p}^{(1)}_{1100}}{\bar{\lambda}_1 - \lambda_0 - \bar{\lambda}_0} - \frac{p^{(0)}_{0200}\bar{p}^{(0)}_{0200}}{2\bar{\lambda}_0 - 4\lambda_0} - \frac{p^{(0)}_{0110}p^{(1)}_{2000}}{2\lambda_1 - 4\lambda_0}, \\
c_{01} =& p^{(0)}_{1011} + \frac{p^{(0)}_{0011}\bar{p}^{(1)}_{0110}}{\lambda_0} + \frac{p^{(0)}_{0011}p^{(1)}_{1010}}{\lambda_0} - \frac{p^{(0)}_{0020}p^{(1)}_{1001}}{\lambda_1 - \bar{\lambda}_1 - \lambda_0} - \frac{p^{(0)}_{1100}\bar{p}^{(0)}_{0011}}{\bar{\lambda}_0 - \lambda_1 - \bar{\lambda}_1} \\
&+ \frac{p^{(0)}_{1010}p^{(0)}_{1001}}{\bar{\lambda}_1} - \frac{p^{(0)}_{2000}p^{(0)}_{0011}}{\lambda_0 - \lambda_1 - \bar{\lambda}_1} - \frac{p^{(0)}_{0002}\bar{p}^{(1)}_{0101}}{\bar{\lambda}_1 - \lambda_1 - \lambda_0} + \frac{p^{(0)}_{1010}p^{(1)}_{0011}}{\bar{\lambda}_1} \\
&- \frac{p^{(0)}_{0101}\bar{p}^{(0)}_{0101}}{\bar{\lambda}_0 - \lambda_0 - \lambda_1} + \frac{p^{(0)}_{0110}\bar{p}^{(0)}_{0110}}{\bar{\lambda}_0 - \lambda_0 - \bar{\lambda}_1} + \frac{p^{(0)}_{0110}p^{(0)}_{1010}}{\lambda_1} + \frac{p^{(0)}_{1001}\bar{p}^{(1)}_{0011}}{\lambda_1},
\end{aligned}
\tag{B.1}
$$

where $p^{(i)}_{klmn} = \partial^{k+l+m+n}p^{(i)}/\partial^k z_0 \partial^l \bar{z}_0 \partial^m z_1 \partial^n \bar{z}_1$ and values of $z_0, \bar{z}_0, z_1, \bar{z}_1$ are taken zero. Coefficients c_{10} and c_{11} can be found using the symmetry $(z_0, \bar{z}_0, z_1, \bar{z}_1) \mapsto ((z_1, \bar{z}_1, z_0, \bar{z}_0)$.

References

Chamara, P.A., Coller, B.D., 2000. Double flutter in an aeroelastic system. AIAA Journal 39, 1206–1208.

Coller, B.D., 2004. Surge/stall interactions in compressors. International Journal of Bifurcation and Chaos, submitted.

Coller, B.D., Chamara, P.A., 2004. Structural nonlinearities and the nature of the classic flutter instability. Journal of Sound and Vibration, in press.

Dowell, E.H., 1975. Aeroelasticity of Plates and Shells. Kluwer, Dordrecht.

Elphick, C., Tirapegui, E., Brachet, M.E., Coullet, P., Iooss, G., 1987. A simple global characterization for normal forms of singular vector fields. Physica D 29, 95–127.

Fung, Y.C., 1993. An Introduction to the Theory of Aeroelasticity. Dover, New York.

Glezer, A., 2000. Flow control using synthetic flows. AIAA Paper 2000–2401.

Guckenheimer, J., Holmes, P.J., 1983. Nonlinear Oscillations, Dynamical Systems and Bifurcations of Vector Fields. Springer, Berlin.

Hall, K.C., 1994. Eigenanalysis of unsteady flows about airfoils, cascades, and wings. AIAA Journal 32, 2426–2432.

Hall, K.C., Thomas, J.P., Dowell, E.H., 2000. Proper orthogonal decomposition technique for transonic unsteady aerodynamic flows. AIAA Journal 38, 1853–1862.

Jahnke, C.C., Culick, F.E.C., 1994. Application of bifurcation theory to the high-angle-of-attack dynamics of the F-14. Journal of Aircraft 31, 26–34.

McKinzie Jr., D.J., 1991. Turbulent boundary layer separation over a rearward facing ramp and its control through mechanical excitation. AIAA Paper 91–0253.

McKinzie, Jr., D.J., 1996. Delay of turbulent boundary layer detachment by mechanical excitation: application to rearward-facing ramp. Technical Report 3541, NASA Technical Paper.

Murray, R.M., Jacobson, C.A., Casas, R., Khibnik, A.I., Johnson, C.R., Bit-Mead, R., Peracchio, A.A., Proscia, W.M., 1997. System identification for limit cycling systems: a case study for combustion instabilities. Technical Report CIT/CDS 97-012, California Institute of Technology, Pasadena, California, USA.

Parekh, D.E., Glezer, A., 2000. Avia: adaptive virtual aerosurface. AIAA Paper 2000–2474.

Poston, T., Stewart, I., 1978. Catastrophe Theory and its Applications. Dover, New York.

Shaw, J., Shaw, S.W., 1989. Instabilities and bifurcations in a rotating shaft. Journal of Sound and Vibration 132, 227–244.

Tang, D.M., Dowell, E.H., Virgin, L., 1998. Limit cycle behavior of an airfoil with a control surface. Journal of Fluids and Structures 12, 839–858.

Wang, X.J., Nicolis, G., 1987. Bifucration phenomena in coupled chemical oscillators: normal form analysis and numerical simulations. Physica D 26, 140–155.

Wiggins, S., 1990. Introduction to Applied Nonlinear Dynamical Systems and Chaos. Springer, New York.